

# Investigation of the Near Acoustic Field of a Ducted Fan

Kyle A. Miller\*, David Morata †, and Dimitri Papamoschou‡  
University of California, Irvine, Irvine, CA, 92697

The acoustic near field of a subscale ducted fan was measured experimentally for the purpose of understanding the physics of sound generation and refining low-order models for aft-emitted tonal fan noise. The experimental rig simulates the fan conditions of an ultra-high-bypass turbofan. Acoustic measurements were performed with a phased array of microphones comprising fixed and scanning sensors, the combination of which offers spatial resolution sufficient to resolve detailed features of the pressure field. Partial-fields decomposition of the signals of axially-scanning sensors shows the potential of recovering the complete harmonic pressure field along the scan line. Axial space-time correlations and azimuthal correlations show trends that are in line with the predictions of a recently proposed source model that is partially informed by internal duct acoustics.

## I. Nomenclature

$a$	=	ambient speed of sound
$\mathcal{D}$	=	decay function
$D_e$	=	fan exit diameter
$\mathbf{G}$	=	cross-spectral matrix
$k_a$	=	acoustic wavenumber
$k_x$	=	axial wavenumber in duct acoustics
$m$	=	azimuthal mode number
$\mathcal{M}$	=	number of microphones
$M_c$	=	convective Mach number
$n$	=	radial mode number
$n_{\text{BPF}}$	=	blade passing frequency harmonic
$p_i(t)$	=	pressure signal of microphone $i$
$P_i(\omega)$	=	Fourier transform of $p_i(t)$
$r$	=	radial coordinate
$R$	=	correlation
$R_o$	=	exit radius of fan nozzle
$t$	=	time
$U_c$	=	convective velocity
$V$	=	sensor speed
$\mathbf{U}, \mathbf{V}$	=	matrices used in singular value decomposition
$x$	=	axial coordinate
$\mathbf{z}, \mathbf{Z}$	=	parameter vectors
$\theta$	=	polar angle
$\kappa_r$	=	radial wavenumber in outward propagation
$\kappa_x$	=	axial wavenumber in outward propagation
$\xi$	=	axial separation
$\mathbf{\Pi}$	=	partial fields vector
$\phi$	=	azimuthal angle
$\Sigma$	=	singular value matrix
$\tau$	=	time shift

---

\*Graduate Student Researcher, Mechanical and Aerospace Engineering, kamille2@uci.edu, Member AIAA.

†Independent Researcher, dmorata@uci.edu, Member AIAA.

‡Professor, Mechanical and Aerospace Engineering, dpamos@uci.edu, Fellow AIAA.

$\omega$  = radian frequency

#### *Subscripts*

$k$  = block index  
 $F$  = fixed microphone  
 $S$  = scanning microphone

#### *Acronyms*

CSM = Cross-Spectral Matrix  
PFD = Partial Fields Decomposition  
VK = Vold-Kalman

## II. Introduction

Propulsion noise of turbofan-powered aircraft comprises primarily fan and jet noise, the former containing tonal components that can dominate the overall noise emissions [1]. To reach NASA's ambitious N+3 community noise goals [2], research on new propulsion systems are centered around the utilization of high-bypass turbofan engines and open rotors [3]. Mitigation of the far-field impact of tonal noise requires careful integration of the engine and airframe and has led to promising aircraft designs such as the blended wing body (BWB) [4].

The number of design parameters for tonal noise suppression through system integration is too large to successfully test all possible configurations. As such, techniques for accurate low-order noise modeling and prediction are needed in the early stages of design to allow for optimized engine noise reduction in both isolated and installed configurations. Current methods for the prediction of sound scattering are readily accessible through programs such as boundary element method (BEM) [5] or the equivalent-source method [6]. However, the proper prediction of scattering and shielding requires the above solvers to have reliable inputs from a source model.

This paper presents a preliminary experimental assessment of a surface-based source model for aft-emitted tonal fan noise. The model was recently introduced by Papamoschou [7] and improvements are presented in a companion paper [8]. The model consists of a collection of coherent linear waveforms on a near-field surface that envelops the fan exhaust. The waveforms contain features of the internal pressure field, as computed by duct acoustics, and can be parameterized. The experimental data includes near field measurements collected on a small-scale ducted fan using a stationary azimuthally-phased array in conjunction with a continuously-scanning linear array to provide high spatial resolution [9–12]. Azimuthal correlations are performed at the peak emission location of each tone to obtain the azimuthal mode number. The harmonic content of the signal was extracted using the Vold-Kalman filter and partial fields decomposition (PFD). PFD also allowed reconstruction of the complex pressure along the scan line for the leading partial field. Space-time correlations were computed along the scan line to measure the axial convective Mach number distribution and compare it to the model prediction.

## III. Methodology

### A. Nature of the Pressure Field

The methodology tools discussed here are generic, but ultimately they will be applied to the tonal content of the noise emitted by a ducted fan. Considering a rotor with  $B$  equally spaced blades rotating at angular speed  $\Omega$ , the emitted radian frequency is

$$\omega = n_{\text{BPF}} B \Omega$$

where  $n_{\text{BPF}}$  is the blade passing frequency harmonic,  $n_{\text{BPF}} = 1$  being the fundamental. The harmonic dependence  $e^{-i\omega t}$  will be assumed throughout, and occasionally this term will be suppressed for brevity.

## B. Space-Time Correlations

Space-time correlations are prevalent in the study of acoustics. Here they are used to extract key features of the near-acoustic field, including the convective velocity and the helical content of the ducted fan exhaust flow. Figure 1 shows a schematic of the sensor deployment used in measuring those correlations. The polar coordinate system  $(x, r, \phi)$  is used, with the axial coordinate  $x$  referenced to the fan exit plane and the azimuthal angle  $\phi$  defined with respect to the downward vertical (the direction away from the pylon of the ducted fan) and being positive counter-clockwise. The sensor radial distance  $r$  is measured from the fan centerline. Considering two sensors at a common radial location  $r$ , the normalized space-time correlation is

$$R(x, \phi; \xi, \Delta\phi, \tau) = \frac{\langle p(x, \phi, t)p(x + \xi, \phi + \Delta\phi, t + \tau) \rangle}{p_{rms}(x, \phi)p_{rms}(x + \xi, \phi + \Delta\phi)} \quad (1)$$

where  $\xi$  is the axial separation,  $\Delta\phi$  is the azimuthal separation,  $t$  denotes the time, and  $\tau$  is the time shift. Axial space-time correlations are obtained by setting  $\Delta\phi = 0$ , while azimuthal space-time correlations are obtained by setting  $\xi = 0$ .

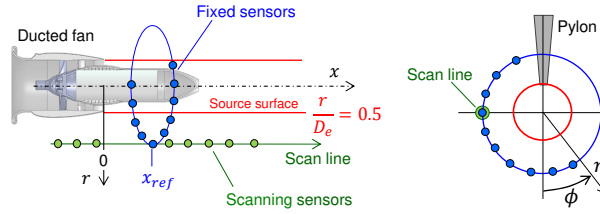


**Fig. 1 Schematic of microphone deployment for the investigation of the near-acoustic field of aft-emitted noise of a ducted fan.**

For a harmonic signal of the type  $p(x, \phi)e^{-i\omega t}$ , where  $p(x, \phi)$  is complex, the space-time correlation reduces to

$$R(x, \phi; \xi, \Delta\phi, \tau) = \frac{p(x, \phi)p^*(x + \xi, \phi + \Delta\phi)}{|p(x, \phi)| |p(x + \xi, \phi + \Delta\phi)|} e^{i\omega\tau} \quad (2)$$

Accurate correlations require good spatial resolution, particularly in the near field where the features of the source can be very small. This constitutes an experimental challenge when the number of sensors is limited. In addition, placing a large number of sensors near the source has the potential of interfering with the emitted acoustic field. In an effort to address these challenges, the axial correlations utilize a linear continuously-scanning microphone array, as depicted in Fig. 1. One sensor is fixed and serves as a reference at location  $x_{ref}$ , while a number  $\mathcal{M}_s$  of sensors traverses continuously in unison. Motion of the sensors introduces non-stationarity in the signal and resulting correlations. This is addressed by dividing the signal into a number of blocks  $K$  within each of which the processes can be considered as quasi-stationary [11, 12]. For a given block  $k$ , the correlation

$$R_{ik}(\tau) = R(x_{ref}; \xi_{ik}, \tau), \quad i = 1, \dots, \mathcal{M}_s$$

is obtained, where  $\xi_{ik}$  is the axial separation of scanning sensor  $i$  from the reference sensor at the center of block  $k$ . The correlation map  $R_{ik}(\tau)$ ,  $i = 1, \dots, \mathcal{M}_s$ ,  $k = 1, \dots, K$  is then synthesized to obtain highly resolved space-time correlations. Azimuthal correlations involved fixed microphones only and were used to assess the helical content of the measured pressure field.

## C. Partial Fields Decomposition

Data from the near-field array were used to decompose the acoustic field along the scan axis into coherent and mutually orthogonal partial fields. The methodology presented in Refs. [10, 12] was used, which represents an extension of Lee and Bolton's original work [13] developed for stationary sensors. The methodology has been successfully utilized in past experimental studies for beamforming of high-speed jets ([10, 12, 14]), and has been used in conjunction with the

boundary element method (BEM) to predict the far-field radiation pattern of screech tones in supersonic underexpanded jets [15]. The key relationships utilized to obtain the partial fields are briefly summarized next.

Consider a set of fixed sensors  $F$  and a set of continuously scanning sensors  $S$ . As described in the previous section, correlations between scanning sensors, or between fixed and scanning sensors, requires division of the signals into  $K$  blocks. The positions of the scanning sensors are computed at the center of each block. A frequency-dependent filter is applied in the estimation of the cross-spectral densities to suppress the effects of non-stationarity, following the guidance in Refs. [11, 12]. For partial fields decomposition, three types of cross-spectral matrices are calculated. First, a reference matrix  $\mathbf{G}_{\text{FF}}$  is constructed based on the full time trace of the fixed sensors only:

$$\mathbf{G}_{\text{FF}}(\omega) = \overline{P_i(\omega)P_j^*(\omega)}, \quad (i, j) \in F \quad (3)$$

where  $\overline{(\cdot)}$  indicates the operation used in spectral averaging and  $*$  is the complex conjugate. For each block  $k$ , we construct a cross-spectral matrix  $\mathbf{G}_{\text{FF},k}$  between the fixed sensors

$$\mathbf{G}_{\text{FF},k}(\omega) = \overline{P_{i,k}(\omega)P_{j,k}^*(\omega)}, \quad (i, j) \in F \quad (4)$$

and a cross-spectral matrix  $\mathbf{G}_{\text{FS},k}$  between fixed and scanning sensors

$$\mathbf{G}_{\text{FS},k}(\omega) = \overline{P_{i,k}(\omega)P_{j,k}^*(\omega)}, \quad i \in F, j \in S \quad (5)$$

The matrices  $\mathbf{G}_{\text{FF}}$  and  $\mathbf{G}_{\text{FF},k}$  have the singular value decompositions

$$\mathbf{G}_{\text{FF}} = \mathbf{U}_{\text{FF}} \mathbf{\Sigma}_{\text{FF}} \mathbf{V}_{\text{FF}}^H \quad (6)$$

and

$$\mathbf{G}_{\text{FF},k} = \mathbf{U}_{\text{FF},k} \mathbf{\Sigma}_{\text{FF},k} \mathbf{V}_{\text{FF},k}^H \quad (7)$$

where superscript  $H$  indicates the complex transpose.

A transfer function matrix between the fixed and scanning sensors is constructed for each block as

$$\mathbf{H}_{\text{FS},k} = \left( \mathbf{G}_{\text{FF},k} \right)^{-1} \mathbf{G}_{\text{FS},k} \quad (8)$$

A potential difficulty with this step is that  $\mathbf{G}_{\text{FF},k}$  may not have an inverse, in which case the Moore-Penrose generalized inverse is used:

$$\left( \mathbf{G}_{\text{FF},k} \right)^{-1} = \left( \mathbf{G}_{\text{FF},k} \right)^\dagger = \mathbf{V}_{\text{FF},k} \mathbf{\Sigma}_{\text{FF},k}^{-1} \mathbf{U}_{\text{FF},k}^H \quad (9)$$

The partial fields for block  $k$  are calculated as

$$\mathbf{\Pi}_k = \mathbf{H}_{\text{FS},k}^T \mathbf{U}_{\text{FF}} \mathbf{\Sigma}_{\text{FF}}^{1/2} \quad (10)$$

where superscript  $T$  indicates the transpose. Recalling that the index  $k$  represents distinct axial positions  $x_k$ , a dense distribution of  $x_k$  along the scan line can be considered as continuous, enabling the approximation

$$\mathbf{\Pi}(x) \approx \mathbf{\Pi}_k \quad (11)$$

The number of orthogonal partial fields obtained with this method equals the number of fixed (reference) microphones used,  $\mathcal{M}_f$ . Following the development of Refs.[10, 16] a global CSM with size  $K\mathcal{M}_s \times K\mathcal{M}_s$ , where  $\mathcal{M}_s$  is the number of scanning sensors, is obtained from

$$\mathbf{G}_{\text{pFD}} = \mathbf{\Pi}_\alpha^H \mathbf{\Pi}_\beta, \quad \alpha, \beta = 1, \dots, K \quad (12)$$

Considering a single partial field  $\Pi(x)$  along the scan line, revolution of the scan line around the fan axis defines a cylindrical surface of radius  $r$  on which the pressure field has the form

$$p(x, r, \phi, t) = \Pi(x) e^{-i\omega t} e^{im\phi} \quad (13)$$

This pressure can be used as a radiation boundary condition in the boundary element method to propagate sound and include its interactions with the airframe [8].

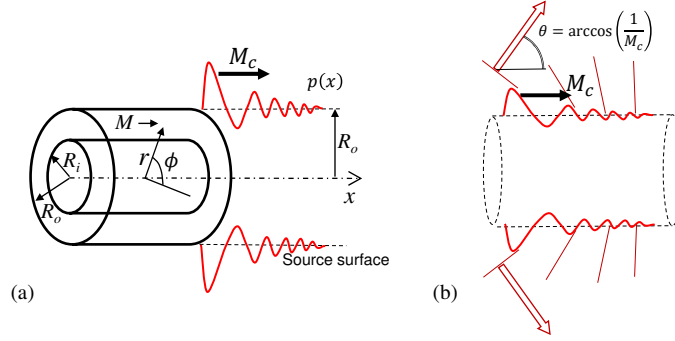


**Fig. 2 (a) Surface-based source model for aft tonal emission; (b) illustration of Mach wave radiation.**

#### D. Noise Source Model

A brief description of the source model for aft tonal emission is provided. The reader is referred to a companion publication for the details [8]. In the analysis that follows the harmonic dependence  $e^{-i\omega t}$  will be suppressed for convenience. The source is prescribed in the form of linear waveforms on a cylindrical surface downstream of the fan exit plane, with radius  $R_o$  equal to that of the fan nozzle at the exit plane. See Fig. 2. The waveforms correspond to cut-on acoustic modes inside the annular duct of the fan. The cut-on modes are denoted  $(m, n)$  where  $m$  is the azimuthal order and  $n$  is the radial mode. The waveforms share the same azimuthal order  $m$  as the cut-on modes. In addition, at the duct exit ( $x = 0$ ) the axial wavenumber of the waveforms matches approximately that of the cut-on modes. This is denoted as the initial axial wavenumber  $k_{xmn}(0)$ . Associated with each waveform is the initial convective Mach number

$$M_{c_{mn}}(0) = \frac{k_a}{k_{xmn}(0)} \quad (14)$$

In analogy with Mach wave emission in supersonic jets, the convective Mach number can be connected to the direction of polar emission via

$$\theta_{mn} = \arccos\left(\frac{1}{M_{c_{mn}}(0)}\right) \quad (15)$$

Temporarily omitting the subscript  $mn$  for brevity, each waveform is assigned the shape

$$p(x, \phi) = A\mathcal{D}(x) \exp[ik_x(x)x + im\phi] \quad (16)$$

here  $A$  is a complex amplitude and  $\mathcal{D}(x)$  is a decay function. The convective Mach number is assumed to decay similarly to the amplitude:

$$M_c(x) = 1 + (M_c(0) - 1)\mathcal{D}(x) \quad (17)$$

and thus reaches the value of 1 at some distance from the nozzle exit. The axial wavenumber is then determined from

$$k_x(x) = \frac{k_a}{M_c(x)} \quad (18)$$

The decay function is selected as

$$\mathcal{D}(x) = \exp\left[-b\left(\frac{x}{R_o}\right)^q\right] \quad (19)$$

where  $b$  and  $q$  are free parameters. Combining Eqs. 14-17, the axial evolution of a given cut-on mode is defined by the parameter vector

$$\mathbf{z} = [A, M_c(0), b, q]$$

Considering now mode  $(m, n)$ , the axial evolution of the waveform is denoted  $p_{mn}(\mathbf{z}_{mn}; x, \phi)$ . The surface-based source is the coherent summation of all the waveforms:

$$p_{\text{source}}(\mathbf{Z}; x, \phi) = \sum_{m,n} p_{mn}(\mathbf{z}_{mn}; x, \phi) \quad (20)$$

where

$$\mathbf{Z} = [\mathbf{z}_{mn}] \quad (21)$$

is the overall parameter vector. Considering that the amplitude  $A$  is complex, the overall parameter vector contains five elements for each mode.

Each waveform  $p_{mn}$  is propagated to a field point  $(x, r, \phi)$  outside the source cylinder. For the cylindrical source surface considered here, the solution to the wave equation gives the emitted pressure field

$$P_{mn}(\mathbf{z}_{mn}; x, r, \phi) = \frac{e^{im\phi}}{2\pi} \int_{-\infty}^{\infty} \widehat{p}_{mn}(\mathbf{z}_{mn}, \kappa_x, \phi) \frac{H_m^{(1)}(\kappa_r r)}{H_m^{(1)}(\kappa_r r_{\text{source}})} e^{i\kappa_x x} d\kappa_x \quad (22)$$

Here  $\kappa_x$  and  $\kappa_r$  are the axial and radial wavenumbers associated with the outward propagation, respectively, and are related to the acoustic wavenumber through  $k_a^2 = \kappa_x^2 + \kappa_r^2$ ;  $\widehat{p}_{mn}$  is the axial Fourier transform of  $p_{mn}$ ; and  $H_m^{(1)}$  is the Hankel function of the first kind of order  $m$ . The complete pressure field is obtained from the superposition

$$p(\mathbf{Z}; x, r, \phi) = \sum_{m,n} P_{mn}(\mathbf{z}_{mn}; x, r, \phi) \quad (23)$$

The cut-on modes for the various harmonics of the ducted fan rig described in the next section were determined using duct acoustics theory [8]. They are listed in Tables 1 and 2 for  $n_{\text{BPF}} = 2$  and 3, respectively. The parameter vector was determined by minimizing the difference between the modeled and experimental cross-spectral densities in the far field [8].

**Table 1. Cut-on modes for  $n_{\text{BPF}} = 2$**

$(m, n)$	(4,1)	(4,2)
$k_x(0)$ ( $\text{m}^{-1}$ )	309	179
$M_c(0)$	1.53	2.64
$\theta$ (deg)	49.2	67.8

**Table 2. Cut-on modes for  $n_{\text{BPF}} = 3$**

$(m, n)$	(-6,1)	(-6,2)	(18,1)
$k_x(0)$ ( $\text{m}^{-1}$ )	462.0	380	246
$M_c(0)$	1.53	1.86	2.87
$\theta$ (deg)	49.2	57.4	69.5

Figure 3 shows results of this parameterization for  $n_{\text{BPF}} = 2$  and 3. For  $n_{\text{BPF}} = 2$ , the dominant waveform, denoted by the black line in the top left subfigure, corresponds to mode (4,1) and has peak radiation at  $\theta = 47^\circ$ . The waveform corresponding to mode (4,2) is denoted by the blue line in the same subfigure; it is much weaker but influences the high polar angles near  $65^\circ$ . For  $n_{\text{BPF}} = 3$  the dominant waveform, denoted by the black line in the top right subfigure, corresponds to mode (18,1) and has peak radiation at  $\theta = 68^\circ$ . The waveforms for modes (-6,1) and (-6,2), denoted by the blue and green lines in the same subfigure, are much weaker and influence the low polar angles. A central question of this study is whether the source formulation based on far-field data can give accurate results in the near field.

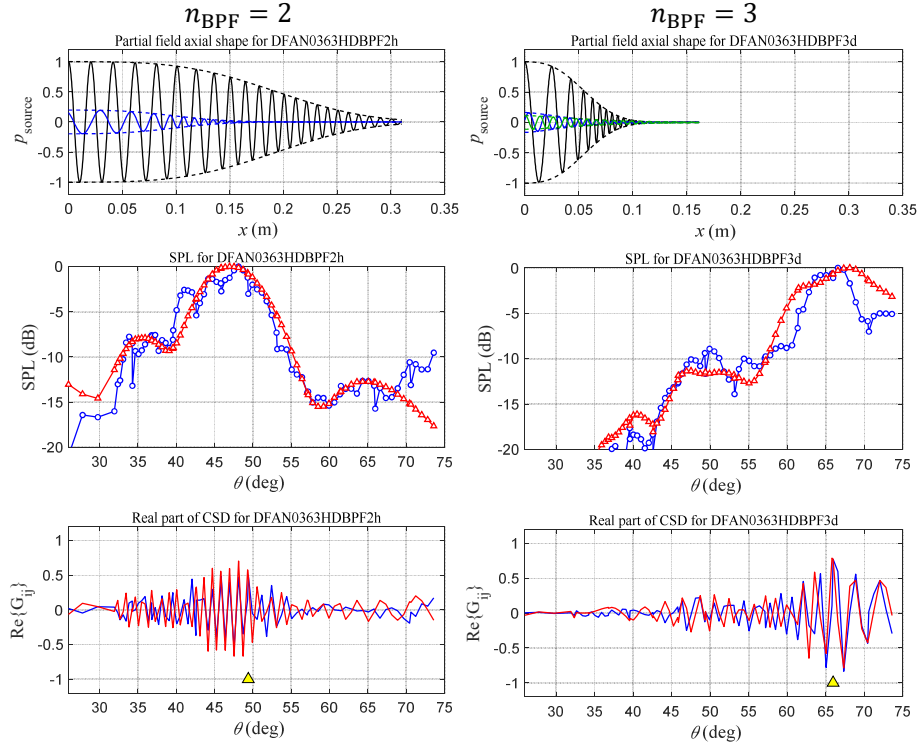


**Fig. 3** Source parameterization based on far-field phased array measurements. Left column:  $n_{\text{BPF}} = 2$ ; right column:  $n_{\text{BPF}} = 3$ . Top row: source waveforms; middle row: directivity of SPL for experiment (blue) and model (red); bottom row: directivity of real part of cross-spectral matrix for experiment (blue) and model (red), with reference sensors at  $\theta = 48^\circ$  and  $66^\circ$  for  $n_{\text{BPF}} = 2$  and  $3$ , respectively. From Ref. [8].

### E. Convective Mach Number

For a fixed radius and azimuthal angle, the pressure of a harmonic signal is expressed as

$$p(x, t) = q(x)e^{-i\omega t}$$

where  $q(x)$  is a complex amplitude. We make the substitution  $q(x) \rightarrow q(x)/|q(x)|$  and compute the normalized space-time correlation as

$$R(x; \xi, \tau) = q(x)q^*(x + \xi)e^{i\omega\tau} = Q(x; \xi)e^{i\omega\tau} \quad (24)$$

where  $Q(x; \xi) = q(x)q^*(x + \xi)$ . On the  $\xi - \tau$  plane, the slope of the line  $R(x; \xi, \tau) = \text{constant}$ , in the vicinity of  $x$  (i.e., for small separation  $\xi$ ), is inversely proportional to the local convective velocity  $U_c(x)$ . Mathematically, we have

$$R(x; \xi, \tau) = \text{constant}$$

and therefore

$$dR(x; \xi, \tau) = 0$$

Expanding around  $x$ ,

$$\frac{\partial R}{\partial \xi} d\xi + \frac{\partial R}{\partial \tau} d\tau = 0$$

The convective velocity is

$$U_c(x) = \frac{d\xi}{d\tau} = -\frac{\partial R / \partial \tau}{\partial R / \partial \xi}$$

Inserting Eq. 24,

$$U_c(x) = -\frac{i\omega Q(x; 0)}{\left[ \frac{\partial Q(x; \xi)}{\partial \xi} \right]_{\xi=0}} \quad (25)$$

The convective Mach number is  $M_c = U_c/a$ , where  $a$  is the ambient speed of sound. The space-time correlations and convective Mach number distributions will be evaluated based on the harmonic pressure fields extracted directly from the experimental signals, computed from PFD, and obtained from the model of Eq. 22.

## IV. Experimental Details

### A. Ducted Fan Setup

The experiments were conducted at the UCI Aeroacoustics Laboratory utilizing a small-scale ducted fan. The model is based on the GE R4 fan with a 14-bladed rotor and 24 stator vanes. The nacelle diameter at the rotor plane is 70 mm and the exit diameter of the fan duct is  $D_e = 74$  mm. The exit-to-inlet area ratio is 0.56. A schematic of the fan is provided in Fig. 4a and its detailed design is outlined in Ref. [3]. The fan is powered by a 6-hp DC brushless motor and yields a fan pressure ratio of 1.15 and tip Mach number of 0.59 when operating at 55000 RPM. For all experiments the operational RPM was kept within 5% of this value. Figure 4b shows a picture of the experimental setup, featuring the near-field phased array described next.

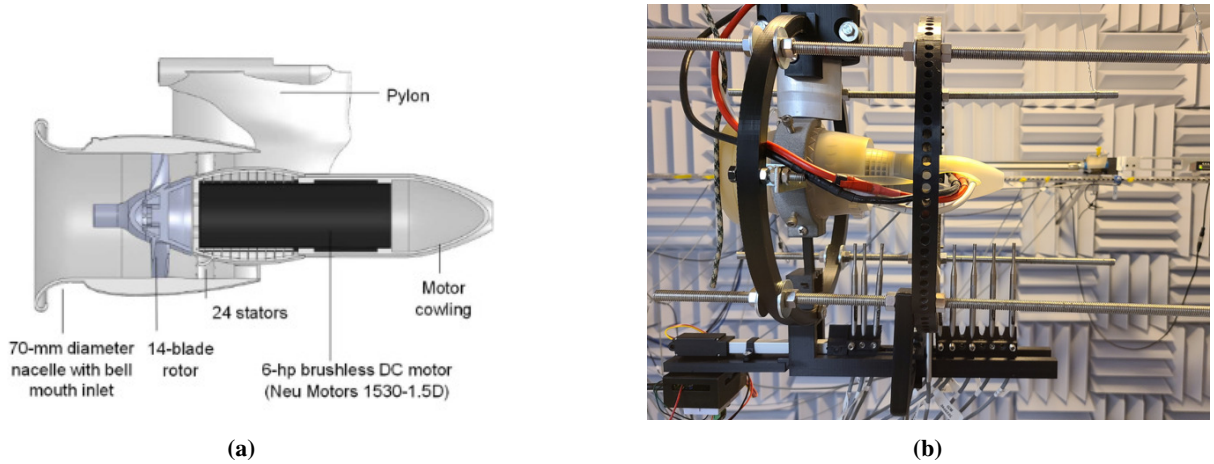


Fig. 4 Small-scale ducted fan rig. (a) Schematic; (b) installation with near field array.

### B. Diagnostics

Acoustic measurements were performed inside an anechoic chamber [8] using Bruel & Kjaer Type 4138 microphones with a frequency response up to 120 kHz. The investigation comprised fixed and scanning microphones. The fixed microphones were installed on an azimuthal holder which could be placed at a variety of axial locations. The scanning microphones traversed as a group along the axial coordinate with a non-dimensional range of  $-0.45 \leq x/D_e \leq 2.25$ . The scanning sensors fore and aft of the azimuthal ring were angled  $5^\circ$  towards the reference sensor to reduce the gap in the scan region caused by the azimuthal ring. One of the (fixed) azimuthal microphones was aligned with the scanning sensors and served as a reference sensor for the space-time correlations.

The microphones were sampled simultaneously at 250 kHz per channel using National Instruments PCI-6143 data acquisition boards. The holder of the axial (scanning) microphones was traversed by an Actuonix L16-P micro linear actuator with a speed  $V=5$  mm/s. The position of each scanning microphone was tracked using the actuator's encoder signal. A tachometer sensor was used to measure the rotational speed of the fan rotor simultaneously with the microphone measurements.

### C. Experimental Protocol

The near-field sensor deployment depicted in Fig. 1 offers a large number of choices on the placement of the axial and azimuthal sensors. To constraint the selection process, it was sought to place the ring of the azimuthal (fixed) sensors near the angle of peak emission as determined by the far-field SPL measurements shown in Fig. 3. This means  $\theta = 47^\circ$  for  $n_{\text{BPF}} = 2$  and  $\theta = 68^\circ$  for  $n_{\text{BPF}} = 3$ .

For the azimuthal correlations, the corresponding normalized coordinates  $(x/D_e, r/D_e)$  for the sensor ring were  $(0.83, 0.88)$  and  $(0.56, 1.53)$ . For the investigation of  $n_{\text{BPF}} = 2$ , 12 sensors were utilized, covering an azimuthal range  $-90^\circ \leq \phi \leq 27^\circ$ . Anticipating much finer features for  $n_{\text{BPF}} = 3$ , 13 sensors were utilized, covering the range  $-30.6^\circ \leq \phi \leq 12.6^\circ$  with a constant spacing of  $3.6^\circ$ . For both sets of experiments, the experimental duration was 2 s over which 500000 samples were acquired.

For the axial correlations, the sensor ring was placed at  $(x/D_e, r/D_e) = (0.55, 1.34)$ , which allowed for the greatest coverage of the axial coordinate while remaining near the regions of peak emission. The sensor on the azimuthal ring at  $\phi = -90^\circ$  (the scan line) served as the reference sensor. Four additional sensors were mounted on the azimuthal holder at  $\phi = -182^\circ, -142^\circ, -99^\circ$  and  $-81^\circ$  and served as references for PFD. Eight scanning sensors were placed on the axially scanning traverse with three sensors fore and five aft of the fixed reference microphones. The axial spacing of the sensors ranged from 10 to 22 mm. The experiment duration was 8 s over which 2000000 samples were acquired. The signal of each sensor was divided into  $K = 40$  blocks with 15% overlap. Each block contained 60000 samples corresponding to a duration of 0.24 s and travel of 1.2 mm. PFD and axial space-time correlations are computed for  $n_{\text{BPF}} = 2$  and  $n_{\text{BPF}} = 3$ , realizing that the location of the reference sensor was not in the direction of peak emission for  $n_{\text{BPF}} = 2$ .

### D. Signal Processing

The Vold-Kalman (VK) filter [17–19] was used to decompose each time trace into harmonic and broadband components, using the tachometer signal for order tracking. For the harmonic component, the complex pressure field was extracted. Example spectra showing the separation of the first three harmonics is provided in Fig. 5. Harmonic content is also obtained from the PFD at the frequency of interest, as described in Section III.C.

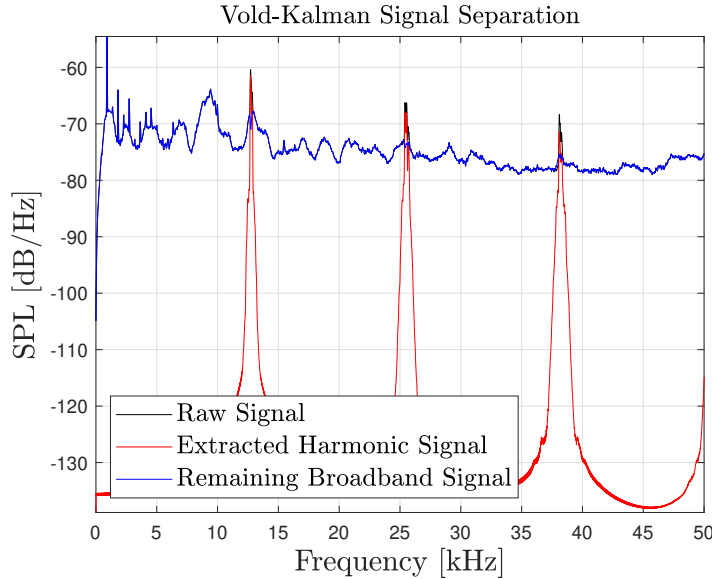


**Fig. 5** Sample of the spectral densities of the original signal and its harmonic and broadband components separated by the Vold-Kalman filter.

Computation of the axial correlations and partial fields can result in non-smooth distributions that complicate further processing, e.g., calculation of the derivative in Eq. 25. In addition, the present axial scanning setup has a spatial gap of about 5 mm near the location of the azimuthal array. The gap is located in a sensitive area of the measurement. It is therefore necessary to interpolate and smooth the signals of interest. Considering a complex signal  $p(x)$  that has a

rapid oscillation, interpolation and smoothing of the real and imaginary parts yields highly unsatisfactory results. To overcome this challenge, the signal was expressed as

$$p(x) = |p(x)|e^{i\psi(x)}$$

where  $\psi(x)$  is the *unwrapped phase*. Interpolation and smoothing of the amplitude  $|p(x)|$  and unwrapped phase  $\psi(x)$  were much more straight-forward and resulted in excellent reconstruction of the signal. The amplitude was reconstructed using a Fourier series and the unwrapped phase was reconstructed using polynomial regression. This approach was applied to the partial field  $\Pi(x)$  and to the axial correlation  $Q(x; \xi)$  based on the VK-filtered signal.

## V. Results

### A. Azimuthal Correlations

Azimuthal correlations are presented for zero time shift ( $\tau = 0$ ). They are plotted for  $n_{\text{BPF}} = 2$  and  $n_{\text{BPF}} = 3$  in Fig. 6. It is recalled that the microphones were placed near the angle of peak emission for each harmonic. For  $n_{\text{BPF}} = 2$  the peak-to-peak spacing of the correlation is  $95.4^\circ$ , which is close to the theoretical spacing of  $90^\circ$  associated with an azimuthal order  $m = 4$  of the cut-on modes determined by duct acoustics. For  $n_{\text{BPF}} = 3$  the peak-to-peak spacing of the correlation is  $21.6^\circ$ . This is close to the theoretical spacing of  $20^\circ$  corresponding to an azimuthal order  $m = 18$ , which relates to cut-on mode (18,1) that dominates far-field emission. These results support the hypothesis that the external pressure field retains the helical content of the cut-on duct modes. It will be assumed throughout the remainder of the paper that the dominant modes have azimuthal orders  $m = 4$  for  $n_{\text{BPF}} = 2$  and  $m = 18$  for  $n_{\text{BPF}} = 3$ .

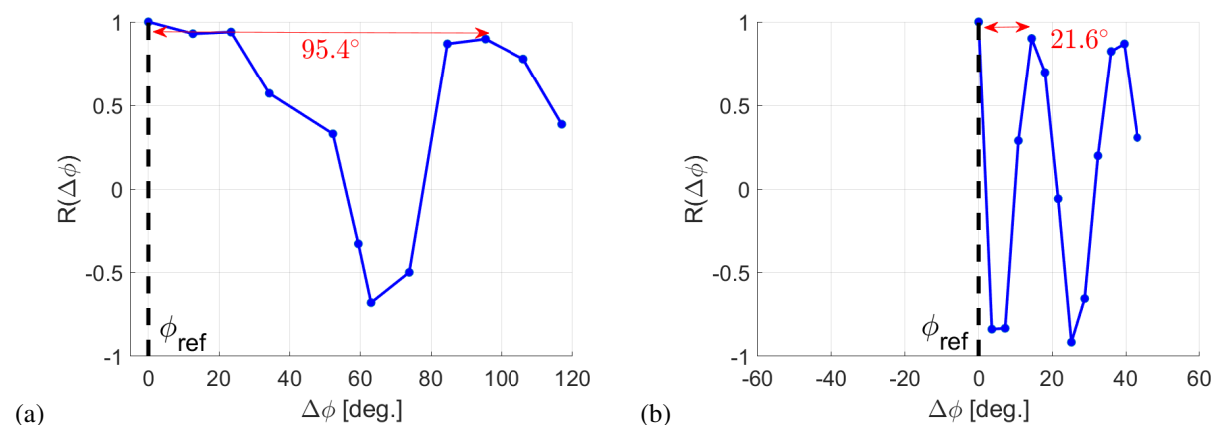


**Fig. 6 (a) Near-field azimuthal correlations. (a)  $n_{\text{BPF}} = 2$ ; (b)  $n_{\text{BPF}} = 3$ . The vertical dashed line indicates the position of the reference sensor.**

### B. Partial Fields Decomposition

Proper evaluation of the global CSM using partial field decomposition requires that a sufficient number of microphones are used to capture the distinct sources within the flow field. The singular values  $\lambda$ , of the reference CSM,  $\Sigma_{\text{FF}}$ , are correlated with the contribution of each source to the flow field. The accuracy of the technique is therefore estimated as the difference between the singular values at the frequencies of interest. The ranked singular values for the axial scanning measurements are shown in Fig. 7 where the  $\Sigma_{\text{FF}}$  matrix was obtained using the sensors on the stationary azimuthal ring. For the second harmonic the leading partial field is sufficiently separated from the remaining partial fields and is insensitive to the number of reference microphones used. For  $n_{\text{BPF}} = 3$ , there is little separation in the partial fields when all reference sensors are used; however, by reducing the number of reference microphones, the singular value separation could be enhanced. Proper placement and utilization of reference sensors requires further investigation; however, due to time constraints was not explored in this investigation. Nonetheless, in an effort to maintain maximal separation of the singular values, calculation of the partial fields for  $n_{\text{BPF}} = 2$  utilized all the reference sensors while the

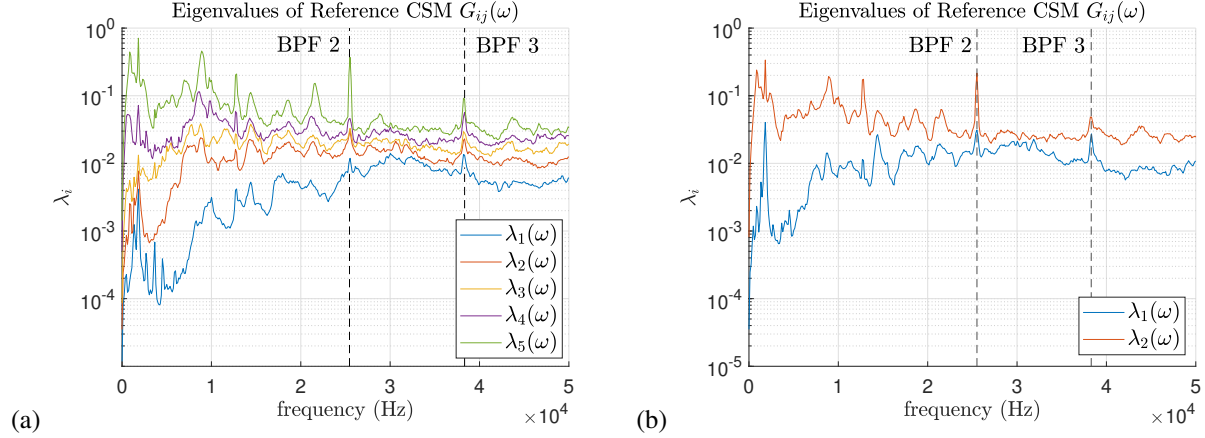


**Fig. 7** Ranked singular values of partial field decomposition (a)  $n_{\text{BPF}} = 2$ ; (b)  $n_{\text{BPF}} = 3$ . The vertical dashed line indicates the frequency of each harmonic.

calculation for  $n_{\text{BPF}} = 3$  utilized only the two reference sensors closest to the scan line (Fig. 7b). For both harmonics, the remaining sections deal only with the leading partial field.

The partial fields obtained from Eq. 10 are fundamental for generating the global CSM used in characterization of the tonal components. Figure 8 plots the leading partial fields for  $n_{\text{BPF}} = 2$  and  $n_{\text{BPF}} = 3$  in their raw form and after reconstruction following the procedures in Section IV.D. Specifically, for each harmonic the figure plots the axial distributions of amplitude, unwrapped phase, and complete partial field before and after reconstruction. It is seen that the reconstruction produces satisfactory smoothing and interpolation across the measurement gap at  $x/D_e = 0.55$ . The resulting distributions are amenable to differentiation for calculating the convective Mach number.

The waveforms prescribed on the model's source surface,  $r/D_e = 0.5$ , are propagated using Eq. 22 to the scan line of the experiments. As with the partial fields, the modeled pressure is decomposed into amplitude and unwrapped phase. The modeled pressure distribution on the scan line is plotted in Fig. 9 along with the reconstructed partial fields. The modeled unwrapped phase is in good agreement with the unwrapped phase of the partial fields for both  $n_{\text{BPF}} = 2$  and  $n_{\text{BPF}} = 3$ . Concerning the amplitude, for  $n_{\text{BPF}} = 2$  the modeled distribution is shifted downstream compared to the experimental one and does not decay as rapidly. For  $n_{\text{BPF}} = 3$ , the modeled and experimental amplitude distributions are generally in good agreement. The complete partial fields reflect the above trends, i.e., a discrepancy in amplitude for  $n_{\text{BPF}} = 2$  and a fairly good match for  $n_{\text{BPF}} = 3$ .

Focusing now on the generation of a radiating surface, the partial fields are modulated azimuthally using Eq. 13 to form a radiation boundary condition on a cylindrical surface. From this surface, one may use linear propagation methods, including the boundary element method, to propagate outwards and include diffraction from airframe surfaces. The real component of the pressure on the radiator surface is presented in Fig. 10. The modeled and experimental pressure fields are in reasonable agreement, with the discrepancies corresponding to those seen in Fig. 9.

### C. Axial Space-Time Correlations

Axial space-time correlations were performed on the scan line  $r/D_e = 1.34$  and  $\phi = -90^\circ$  using Eq. 2. The reference sensor was placed at  $x_{\text{ref}}/D_e = 0.55$ . Three types of pressures were used: the measured pressure after VK filtering; the pressure of the reconstructed partial field as depicted in Fig. 8; and the modeled pressure as shown in Fig. 9. The correlation resulting from the VK-filtered pressure underwent the reconstructions procedures of Section IV.D. The correlations are presented in the normalized coordinates  $x/D_e = (x_{\text{ref}} + \xi)/D_e$  and  $\tau a/D_e$ . Figure 11 plots isocontours of  $R(x/D_e, \tau a/D_e)$  for the aforementioned pressures and for  $n_{\text{BPF}} = 2$  and 3. The experimental correlations using the VK-filtered signal and the partial fields are very close, and the modeled correlations are in general agreement with the experimental ones. For axial locations close to the reference sensor, the slope of the isoline  $R(x/D_e, \tau a/D_e) = \text{const.}$  is inversely proportional to the convective Mach number  $M_c$ . A slope of 1 indicates waves propagating from left to right with the speed of sound. For all cases the contour slope is near zero around  $x = 0$ , indicating wavefronts that are traveling laterally with respect to the fan axis and whose trace along the scan line propagates at near-infinite speeds. The propagation speed declines with downstream distance, reaching near sonic speed at far downstream locations.

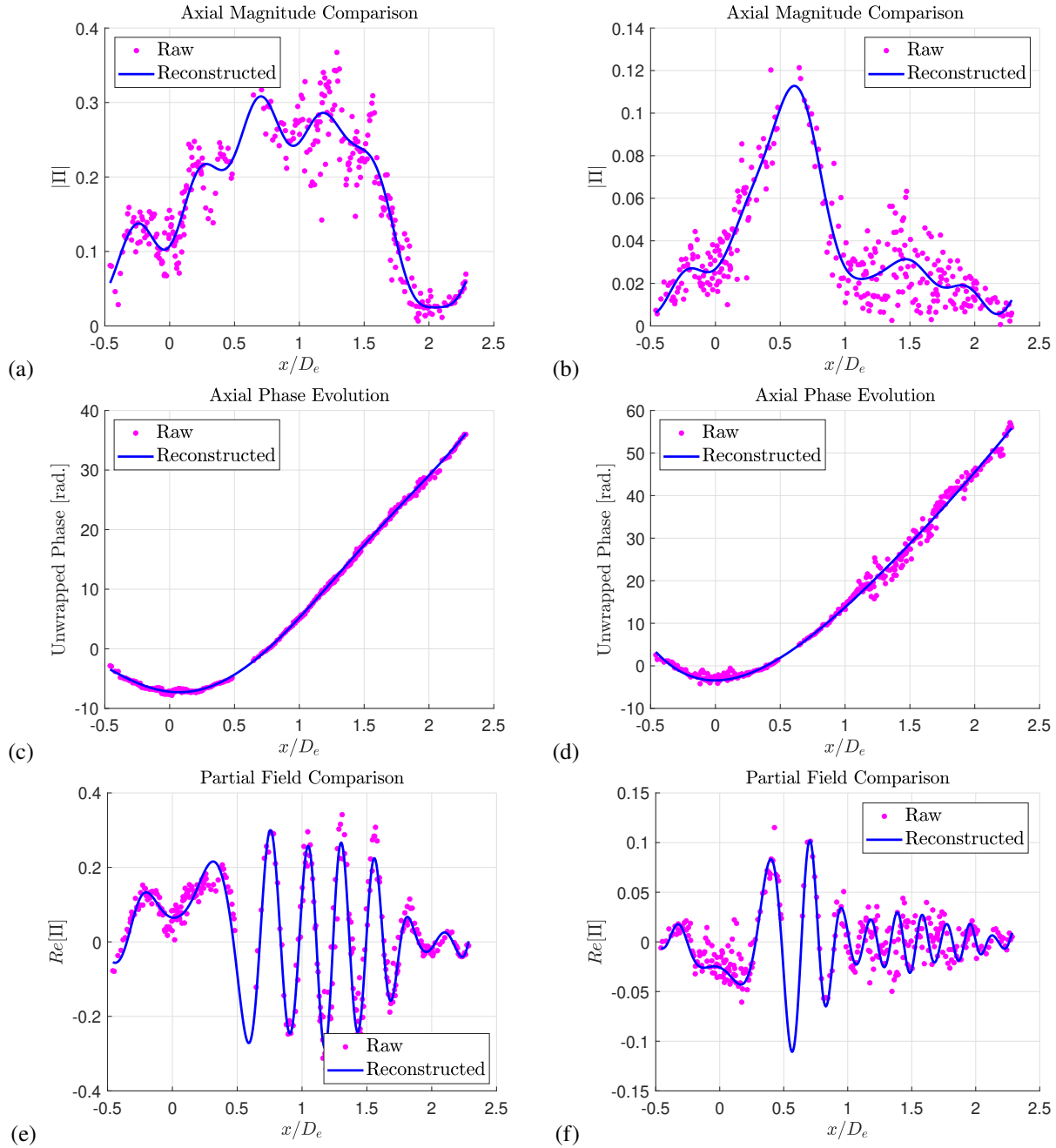


**Fig. 8** Axial distributions along scan line of leading partial fields and their components. Left column:  $n_{\text{BPF}} = 2$ ; right column:  $n_{\text{BPF}} = 3$ . Top row: amplitude; middle row: unwrapped phase; bottom row: real part of complete partial field. Symbols indicate raw distributions and solid lines depict their reconstruction.

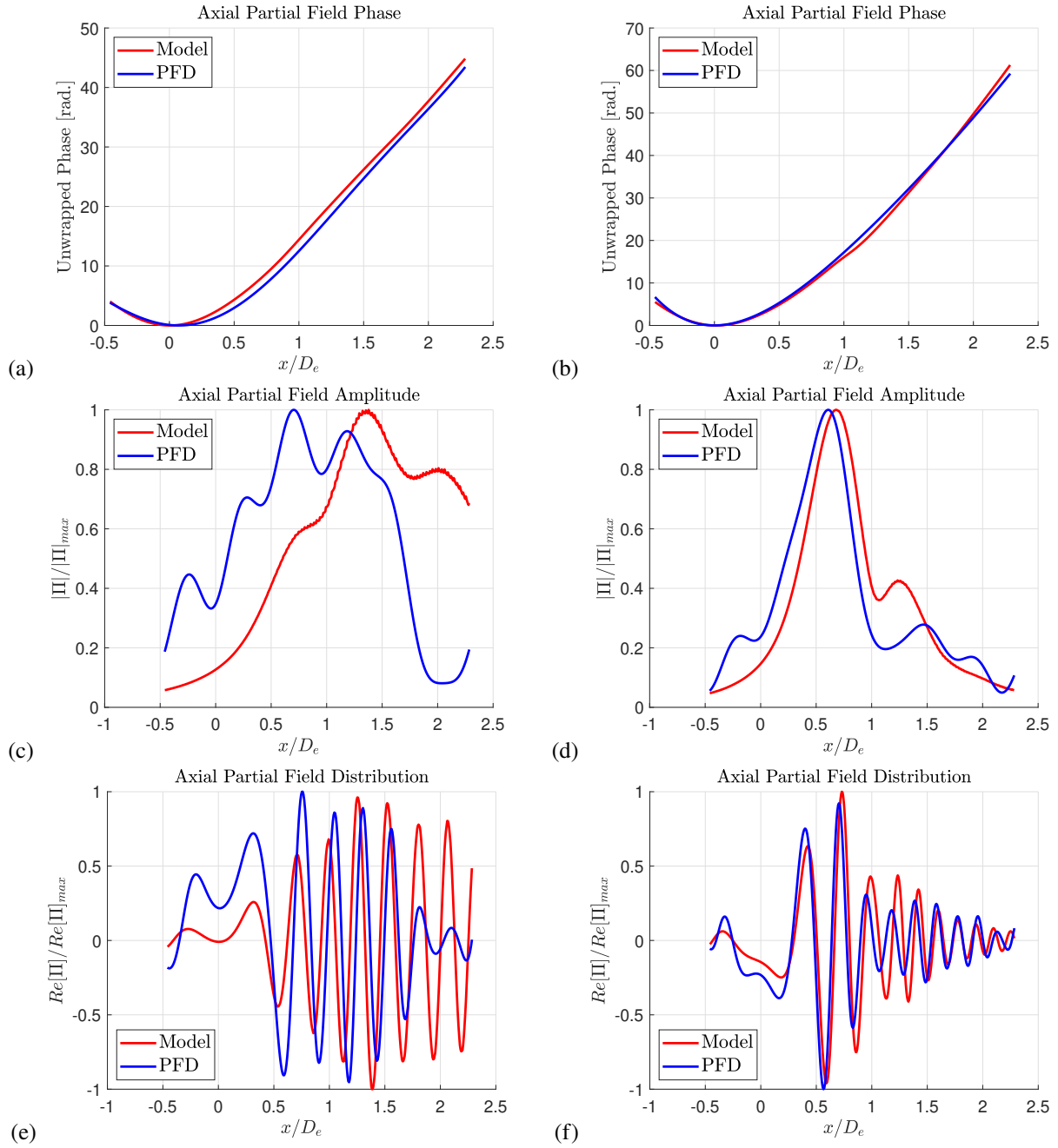


**Fig. 9** Axial distributions along scan line of modeled (red lines) and experimental (blue lines) pressures, the latter based on the reconstructed partial fields. Left column:  $n_{\text{BPF}} = 2$ ; right column:  $n_{\text{BPF}} = 3$ . Top row: unwrapped phase; middle row: amplitude; bottom row: real part of pressure.

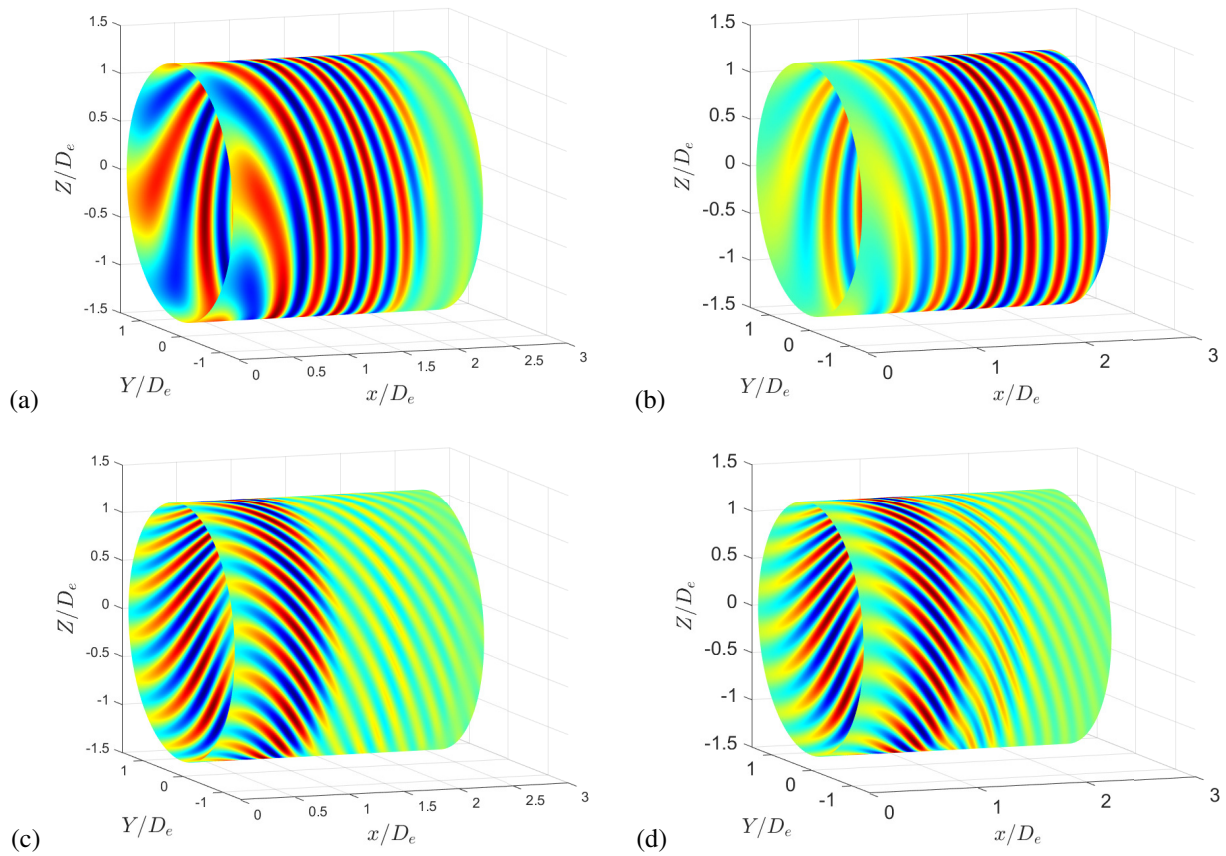


**Fig. 10** Pressure distributions on a cylindrical radiator surface. Left column: measured; right column: modeled. Top row:  $n_{\text{BPF}} = 2$ ; bottom row:  $n_{\text{BPF}} = 3$ .

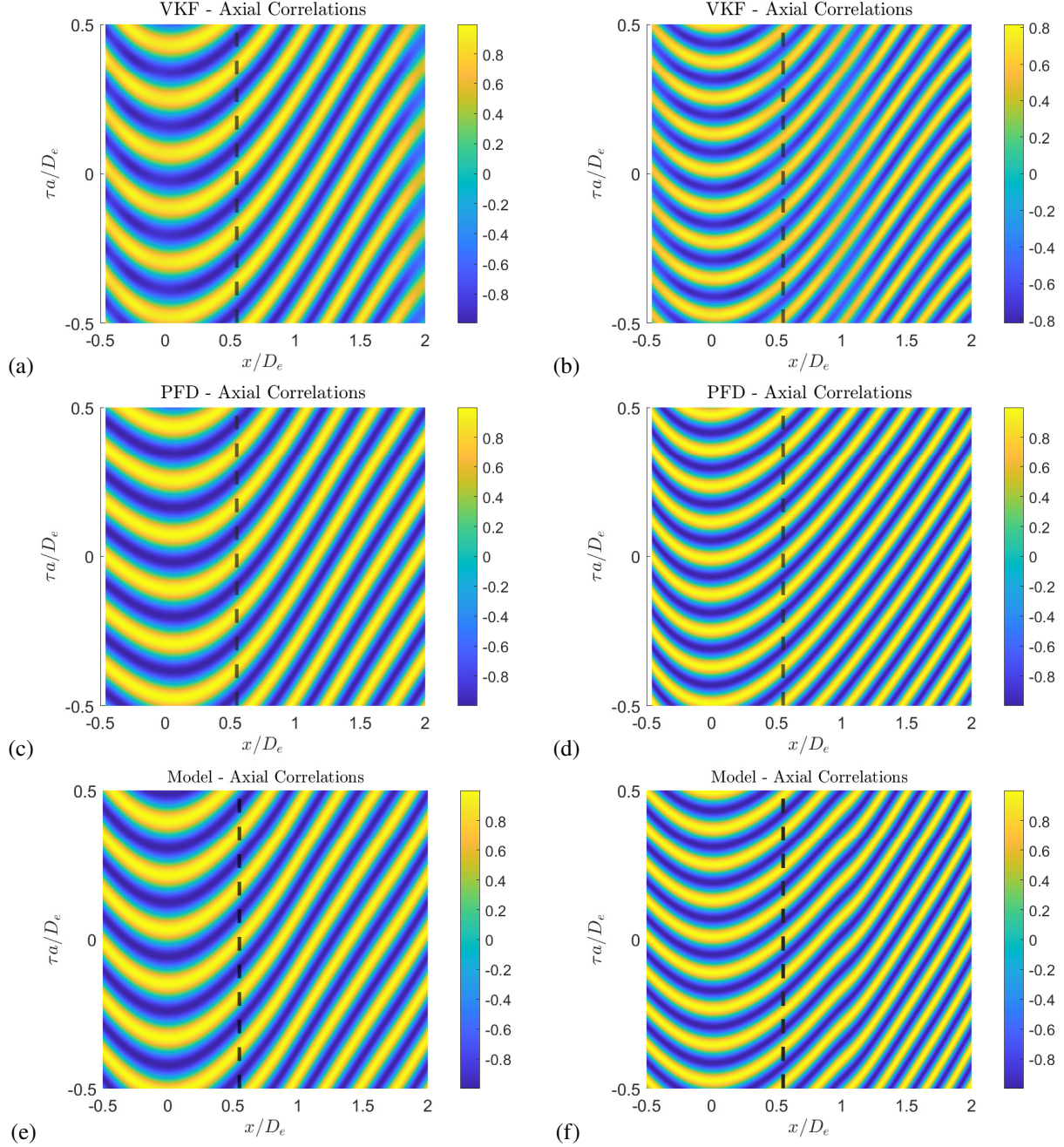


**Fig. 11** Isocontours of space-time correlations on the scan line with reference sensor at  $x_{\text{ref}}/D_e = 0.55$  (vertical dashed lines). Left column:  $n_{\text{BPF}} = 2$ ; right column:  $n_{\text{BPF}} = 3$ . Top row: VK-filtered signal; middle row: reconstructed partial field; bottom row: model.

#### D. Convective Mach Number

The qualitative agreement of the modeled and experimental space-time correlations seen in Fig. 11 motivated a quantitative assessment of the convective velocity using Eq.25. As explained in Section III.E, the convective velocity  $U_c(x)$  is computed from the axial space-time correlation at reference point  $x$  for small displacement  $\xi$ . An important attribute of the PFD in conjunction with the continuous-scan paradigm is that each partial field is finely resolved enough to allow computation of  $U_c(x)$  throughout the entire scan line. In contrast, the raw microphone signals allow space-time correlations between the scanning sensors and between the scanning sensors and the fixed (reference)

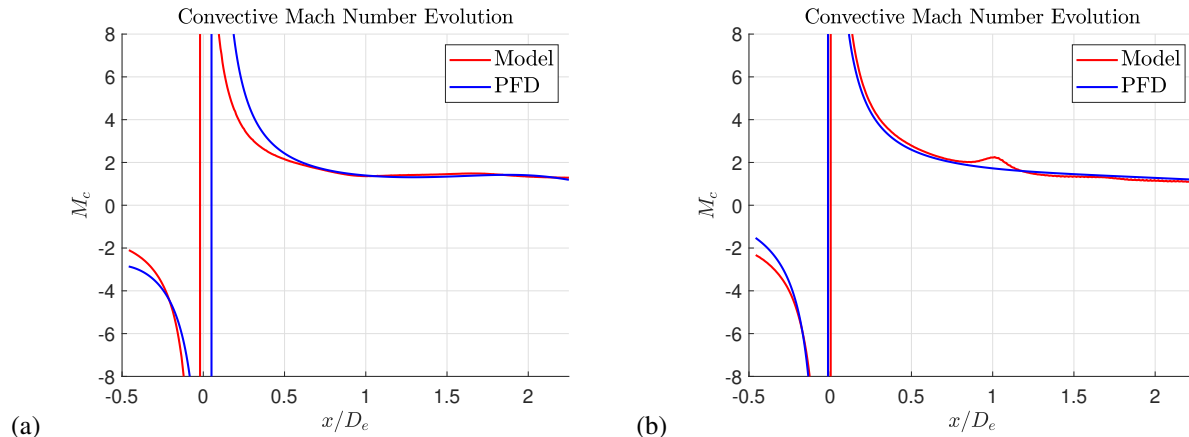


**Fig. 12 Axial distribution of convective Mach number on the scan line based on experiment (leading partial field) and model. (a)  $n_{\text{BPF}} = 2$ ; (b)  $n_{\text{BPF}} = 3$ .**

sensor located at  $x_{\text{ref}}$ . In the former case, the spatial separation  $\xi$  (i.e., the distance between scanning sensors) is too coarse to accurately determine  $U_c(x)$ ; in the latter scenario, only  $U_c(x_{\text{ref}})$  can be determined. The harmonic signals emerging from VK-filtering allow theoretically the possibility of relaxing these limitations, but this was not thoroughly investigated.

Here the experimental  $M_c(x) = U_c(x)/a$  was evaluated using the leading partial field and its distribution was compared to that predicted by the model. These distributions are presented in Fig. 12. The overall trends between model and experiment are consistent, showing near-infinite  $M_c$  near  $x = 0$  (indicating lateral propagation of acoustic waves), negative  $M_c$  for  $x < 0$  (upstream propagation), and rapidly declining, positive  $M_c$  for  $x > 0$ . For  $n_{\text{BPF}} = 2$ , the model overpredicts the rate of decline for  $x/D_e < 0.5$  but matches well the experiment downstream, both distributions reaching  $M_c \approx 1.2$  at  $x/D_e = 2.25$ . For  $n_{\text{BPF}} = 3$  the modeled and experimental distributions are in very close agreement throughout the surveyed region. Recalling that the model was calibrated based on far-field acoustic data, the agreement seen in Fig. 12 provides encouragement that the model captures the fundamental physics of noise emission.

## VI. Concluding Remarks

The near acoustic field of a small-scale ducted fan was surveyed using a microphone phased array that combined azimuthal and axial deployments of sensors. A group of sensors traversed continuously in the axial direction, enabling resolution of the fine spatial features of the pressure field. The investigation focused on tonal noise emitted in the aft direction at the second and third harmonics of the blade passing frequency ( $n_{\text{BPF}} = 2$  and 3). The results were compared to a recently proposed model where the source features are informed by the internal duct acoustics.

Signal processing included extraction of the harmonic content using the Vold-Kalman filter, partial fields decomposition (PFD), azimuthal correlations, and space-time correlations in the axial direction. The azimuthal correlations of the harmonic signals indicated azimuthal orders consistent with those inferred from internal duct acoustics for the strongest modes. For each harmonic, the PFD enables reconstruction of the complex pressure along the line of the scanning sensors. These distributions have the characteristics of amplitude modulated traveling waves and can be used to generate a cylindrical “radiator” surface for propagating to the far field. The modeled pressure distribution matches well the experimental one at  $n_{\text{BPF}} = 3$  but deviates somewhat for  $n_{\text{BPF}} = 2$ . Space-time correlations along the scan line show good qualitative agreement between model and experiment. The convective Mach number  $M_c$  based on the space-time correlations was computed for the experimental and modeled complex pressures. Both distributions show a rapid decay of  $M_c$  with downstream distance, plateauing near a value of 1.2 at the end of the region surveyed. The model shows a very good match to the experimental distribution at  $n_{\text{BPF}} = 3$  while it overpredicts the decay rate for  $n_{\text{BPF}} = 2$ .

The investigation provides valuable guidance for refining the model, which may include additional free parameters. In addition, lessons learned in the conduct of the experiments will lead to better protocols regarding the optimal placement and traversing of sensors for mapping the key features of the acoustic near field.

## Acknowledgments

This work was supported by NASA Phase II Small Business Innovation Research (SBIR) contract 80NSSC20C0089 under technical monitor Dr. David Stephens of NASA GRC. ATA Engineering, Inc. was the prime.

## References

- [1] Krejsa, E., and Stone, J., “Enhanced Fan Noise Modeling for Turbofan Engines,” *NASA/CR-2014-218421*, 2014.
- [2] Jones, S., Haller, W., and Tong, M., “An N+3 Technology Level Reference Propulsion System,” *NASA/TM-2017-219501*, 2017.
- [3] Truong, A., and Papamoschou, D., “Experimental Simulation of Ducted Fan Acoustics at Very Small Scale,” *AIAA Paper 2014-0718*, 2014. <https://doi.org/10.2514/6.2014-0718>.
- [4] Liebeck, R., “Design of the Blended Wing Body Subsonic Transport,” *Journal of Aircraft*, Vol. 41, No. 1, 2004, pp. 10–25. <https://doi.org/10.2514/1.9084>.
- [5] Papamoschou, D., “Prediction of Jet Noise Shielding,” *AIAA Paper 2010-0653*, 2010. <https://doi.org/10.2514/6.2010-653>.
- [6] Nark, D., Burley, C., Tinetti, A., and Rawls, J., “Initial Integration of Noise Prediction Tools for Acoustic Scattering Effect,” *AIAA Paper 2008-2996*, 2009. <https://doi.org/10.2514/6.2008-2996>.
- [7] Papamoschou, D., “Modeling of Aft-Emitted Tonal Fan Noise in Isolated and Installed Configurations,” *AIAA Paper 2021-0009*, 2021. <https://doi.org/10.2514/6.2021-0009>.
- [8] Papamoschou, D., “Improved Modeling of Aft-Emitted Tonal Noise from a Ducted Fan,” *Abstract submitted to AIAA Aviation 2023*, 2023.
- [9] Shah, P., Vold, H., Hensley, D., Envia, E., and Stephens, D., “A High-Resolution Continuous-Scan Acoustic Measurement Method for Turbofan Engine Applications,” *Journal of Turbomachinery*, Vol. 137, 2015, pp. 121002–121002–11. <https://doi.org/10.1115/1.4031341>.
- [10] Shah, P. N., White, A., Hensley, D., Papamoschou, D., and Vold, H., “Continuous-Scan Phased Array Measurement Methods for Turbofan Engine Acoustic Testing,” *Journal of Engineering for Gas Turbines and Power*, Vol. 141, No. 8, 2019. <https://doi.org/10.1115/1.4042395>.
- [11] Papamoschou, D., Morata, D., and Shah, P., “Inverse Acoustic Methodology for Continuous-Scan Phased Arrays,” *AIAA Journal*, Vol. 57, No. 12, 2019, pp. 5126–5141. <https://doi.org/10.2514/1.J058085>.
- [12] Morata, D., and Papamoschou, D., “High-Resolution Continuous-Scan Beamforming,” *AIAA Journal*, Vol. 61, No. 1, 2022, pp. 1–15. <https://doi.org/10.2514/1.J061910>.
- [13] Lee, M., and Bolton, J. S., “Scan-Based Near-Field Acoustical Holography and Partial Field Decomposition in the Presence of Noise and Source Level Variation,” *The Journal of the Acoustical Society of America*, Vol. 119, No. 1, 2006, pp. 382–393. <https://doi.org/10.1121/1.2133717>.
- [14] Shah, P. N., and Papamoschou, D., “Characterization of High Speed Jet Acoustics Using High-Resolution Multi-Reference Continuous-Scan Acoustic Measurements on a Linear Array,” *AIAA Paper 2020-0005*, 2020. <https://doi.org/10.2514/6.2020-0005>.
- [15] Morata, D., Miller, K. A., and Papamoschou, D., “Experimental Study of Underexpanded Screeching Jet and Its Interaction with Upstream Reflector,” *AIAA Paper 2022-2868*, 2022. <https://doi.org/10.2514/6.2022-2868>.
- [16] Morata, D., and Papamoschou, D., “Extension of Traditional Beamforming Methods to the Continuous-Scan Paradigm,” *AIAA Paper 2022-1154*, 2022. <https://doi.org/10.2514/6.2022-1154>.
- [17] Vold, H., and Leuridian, J., “High Resolution Order Tracking at Extreme Slew Rates Using Kalman Tracking Filters,” *SAE Technical Paper 931288*, 1993. <https://doi.org/10.4271/931288>.
- [18] Stephens, D., and Vold, H., “Order Tracking Signal Processing for Open Rotor Acoustics,” *Journal of Sound and Vibration*, Vol. 333, 2014, pp. 3818–3830. <https://doi.org/10.1016/j.jsv.2014.04.005>.
- [19] Truong, A., and Papamoschou, D., “Harmonic and Broadband Separation of Noise from a Small Ducted Fan,” *AIAA Paper 2015-3282*, 2015. <https://doi.org/10.2514/6.2015-3282>.